Crystal growth of lead carbonates: Influence of the medium and relationship between structure and habit

Antonio Sánchez-Navas [a,d,*], Olimpia López-Cruz [b], Nicolás Velilla [a], Isaac Vidal [c]

[a] Departamento de Mineralogía y Petrología, Facultad de Ciencias, Universidad de Granada, 18071 Granada, Spain
[b] Departamento de Pintura, Facultad de Bellas Artes, Universidad de Granada, 18071 Granada, Spain
[c] Grupo de Modelización y Diseño Molecular, Departamento de Química Orgánica, Facultad de Ciencias, Universidad de Granada, 18071 Granada, Spain
[d] IACT-CSIC, University of Granada, Granada, Spain

ARTICLE INFO

ABSTRACT

The crystal-growth features of cerussite and hydrocerussite formed by two different chemical reactions are studied. With respect to the former, acid-vapour oxidation and latter carbonation of metallic lead produced a nanocrystalline precipitate for the lead carbonates. In the latter, cerussite and hydrocerusite are precipitated after mixing two mother solutions in liquid and solid porous media, forming diverse polyhedral morphologies. Crystal growth in gel medium gives rise to pseudo-cubic morphologies by the aggregation of one-micron-sized particles of cerussite. Skeletal morphologies composed of cyclically twinned crystals of cerussite also occur in gel-growth experiments. These morphologies were determined by kinetic factors, in particular by high supersaturation conditions that led to high growth rates. Kinetics also favoured the predominance of weak over strong interactions during crystal growth. The habit observed for cerussite crystals has been explained based on crystal-structure considerations and quantum-mechanical calculations. In particular, the crystal growth along the a direction in cyclically twinned crystals is explained by the binding forces between the CO_3^{2-} molecular group and Pb^{2+}, defining an uninterrupted chain of strong bonds along that direction. However, the preferred growth along the c direction observed for the cerussite crystal formed in gel media is here attributed to an intermolecular interaction through C–C bonds. The occurrence of a chemical bonding between the C atoms of the CO_3^{2-} molecular groups aligned along the c direction is clearly shown by the theoretical analysis of the electron density with the quantum theory of atoms in molecules (QTAIM).

© 2013 Elsevier B.V. All rights reserved.

1. Introduction

Historically, the precipitation of carbonate of lead or white lead begun with the Greeks and Romans from metallic lead and vinegar, as described in the Vitruvius's books and in the Pliny's *Natural History* [1,2]. Carbonate of lead consists mainly of two chemical compounds: cerussite (chemical formula: $PbCO_3$, space group: *Pmcn*, lattice parameters: $a=5.15$ Å, $b=8.47$ Å, $c=6.11$ Å [3]) and hydrocerussite (chemical formula: $Pb_3(CO_3)_2(OH)_2$, space group: $R3m$, lattice parameters: $a=5.25$ Å and $c=23.70$ Å [4]). Both compounds occur as minerals in nature and constitute alteration products of native and primary lead ores [5]. Cerussite and hydrocerussite also occur in soils from weathering or oxidation processes of metallic Pb bullets, at recycling sites for lead-acid batteries, at Pb-smelting sites, and in household plumbing from lead corrosion by drinking water [6–9].

The chemical equilibrium between cerussite and hydrocerussite has been broadly studied from a geochemical standpoint [10–12]. The chemical reaction relating cerussite and hydrocerussite is: $3PbCO_3(s) + H_2O(l) \leftrightarrow Pb_3(CO_3)_2(OH)_2(s) + CO_2(g)$. According to this reaction the effect of water dilution at the Earth's surface involves a decrease in the atmospheric P_{CO_2} ($10^{-3.5}$ atm), which would favour the precipitation of hydrocerussite under ambient conditions. Moreover, hydrocerussite is considerably less soluble than cerussite at pH > 7.0, where the values of the partial pressure of CO_2 are clearly less than $10^{-3.5}$ atm [11]. Randall and Spencer [13] indicated that cerussite is unstable relative to hydrocerussite at P_{CO_2} of less than $10^{-1.8}$ atm. However, hydrocerussite, relative to cerussite, is rare in soils, leading Garrels [12] to conclude that hydrocerussite must be stable at much lower P_{CO_2} values (less than 10^{-4} atm) to account for the scarcity of hydrocerussite relative to cerussite on the Earth's surface.

More than 50 forms have been detected on cerussite crystals, the most important being: {0 1 0}, {1 1 0}, {1 1 1}, {0 2 1}, {0 0 1}, {0 1 2}, {1 0 0}, {0 1 1}, {1 3 0}, and {1 0 2} [14–17]. The relative development of some of these forms is responsible for four main habits of cerussite crystals formed in the laboratory and in natural
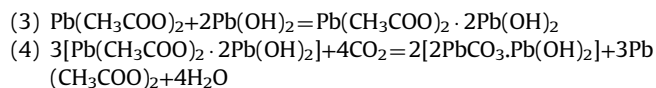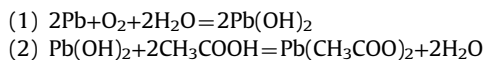
deposits: (1) pseudohexagonal habits resulting from the combination of {1 1 1}, {0 2 1}, {1 1 0}, and {0 1 0} forms; (2) elongated crystals in the direction of the *a* crystallographic axis; (3) tabular crystals according to (0 1 0); and (4) triplet crystals with cyclic twinning, with a twin plane parallel to the face (1 1 0). Cyclic twinning in cerussite is equivalent to that frequently found in aragonite, which is isostructural with cerussite. Hydrocerussite usually forms tabular hexagonal crystals with the faces of {0 0 1} pinacoid prevailing over those of {1 1 2} and {1 1 4} hexagonal bipyramids [18–21].

Here, we examine the precipitation of lead carbonates by solution growth, gel growth, and vapour growth. Two main thrusts of this work concern: (1) the kinetic aspects of crystal growth of lead carbonates precipitated by different methods, including historical ones; and (2) the structural aspects of crystal growth as deduced from the interpretation of polyhedral morphologies detected for cerussite in our experiments. The primary aim of our investigation is to evaluate the influence of the medium on the crystal-growth features of the cerussite and hydrocerussite grown in the diverse precipitation experiments. A thorough investigation of the structural aspects of crystal growth reveals that the morphology of crystals can be successfully used to find new bonding interactions in crystals. For this, the electronic properties of cerussite have been studied theoretically with quantum-mechanical calculations using the density functional theory (DFT) and the quantum theory of atoms in molecules (QTAIM) in order to establish a relationship between the structure and the habit of cerussite.

2. Experimental

2.1. Biomediated and inorganic vapour growth

Hydrocerussite and cerussite was precipitated using the historical method of manufacturing known as the "stack" or "Dutch" process whereby metallic lead is first oxidized by acetic acid vapours in the presence of moisture, and the resulting lead acetate intermediate is later transformed into lead carbonate by the action of carbon dioxide. Diverse sources of carbon dioxide were used: commercial gas cylinders, manure, and liquid bacterial culture medium (Table 1). The latter contained bacteria of the genus *Acetobacter*, which made volatile acetic acid in the form of wine vinegar. *Acetobacter* can finally oxidize acetic acid to carbon dioxide and water. In the biomediated processes, aerobic bacteria metabolise nitrogenated organic matter (proteins) with the subsequent production of CO_2 and NH_3. Ammonia gas increases the basicity of the precipitation medium, favouring the formation of hydrocerussite. The chemical reactions leading to the formation of the hydroxide lead carbonate (hydrocerussite) occur as follows [22]:

(1) $2Pb + O_2 + 2H_2O = 2Pb(OH)_2$
(2) $Pb(OH)_2 + 2CH_3COOH = Pb(CH_3COO)_2 + 2H_2O$
(3) $Pb(CH_3COO)_2 + 2Pb(OH)_2 = Pb(CH_3COO)_2 \cdot 2Pb(OH)_2$
(4) $3[Pb(CH_3COO)_2 \cdot 2Pb(OH)_2] + 4CO_2 = 2[2PbCO_3 \cdot Pb(OH)_2] + 3Pb(CH_3COO)_2 + 4H_2O$

2.2. Solution and gel growth

Solution growth of $PbCO_3$ was carried out by bulk crystallization (free-drift experiments) where two solutions of relatively easily dissolved salts (25 mM $NaHCO_3$, 25 mM $Pb(CH_3COO)_2 \cdot 3H_2O$) are mixed (Table 1). The resulting solution becomes supersaturated with respect to the less soluble $PbCO_3$ substance.

Gel growth of cerussite and hydrocerussite was performed by the counter-diffusion of carbonate solutions *vs.* lead nitrate solutions through a column of silica gel (stock solutions, 1.0 M, of Na_2CO_3, and $Pb(NO_3)_2$, Table 1). The silica gel of pH 5.5 was prepared by acidification of sodium silicate solution with 1 N HCl [23]. It was poured into a U-tube and allowed to polymerize to a solid gel.

2.3. Analytical techniques

The precipitates were analysed by X-ray diffraction (XRD) using a PANalytical X'Pert Pro diffractometer (Cu K_α radiation, 45 kV, 40 mA) equipped with an X'Celerator solid-state lineal detector. XRD diagrams were obtained from the genuine precipitates, *i.e.* from non-milled samples, deposited in a sample holder with no background noise. This was made of a single crystal silicon cut at special orientation to produce a zero-diffraction plate. The sample holder was also spun, the spinning rate being adjusted in such a way as to improve the quality of the diffraction data. The diffraction patterns were determined using a continuous scan between 3–50°2θ and 0.01°2θ of step size, 20 s of time step, and a scan speed of 3°2θ per min. The data were processed using the XPowder® software [24].

Single-point Raman spectra of cerussite aggregates were collected using a JASCO NRS-5100 confocal microRaman spectrometer equipped with an 1800 line mm^{-1} grating monochromator, a Peltier-cooled CCD Detector, and Olympus objective lenses. The excitation source was a 532 solid-state laser operating at 0.7 mW output power. An objective lens (N.A.=0.9) of $100 \times$ magnification was used. Raman spectra, with 2 cm^{-1} of spectral resolution, were recorded in the range 100–1200 cm^{-1} using integration times of 10 s per accumulation over two accumulations. The spectra were calibrated with respect to the 520 cm^{-1} line of a silicon plate.

Crystal-growth features and crystallographic relations of cerussite and hydrocerussite were investigated with a high-resolution field-emission scanning electron microscope (FESEM) LEO GEMINI 1525 equipped with an Oxford Instruments EBSD detector and the Inca Crystal software (CIC, Granada University, Spain). Electron back-scattered diffraction (EBSD) analysis provided information on the orientation of the cerussite crystal lattice and enabled the

Table 1
Type of medium, reactants, times for growth, morphologies observed in SEM images and mineralogy of precipitates determined by XRD.

	Biomediated experiments		Inorganic experiments		
	Vapour growth		Vapour growth	Solution growth	Gel growth
Reactants	Pb rod, $P_{CO_2} \approx 10^{-3.5}$ atm (atmospheric), $P_{CH3COOH}$?		Pb rod, $P_{CO_2} \approx 1$ atm, $P_{CH3COOH}$?	25 mM $NaHCO_3$, 25 mM Pb $(CH_3COO)_2 \cdot 3 H_2O$	1 M Na_2CO_3, 1 M $Pb(NO_3)_2$
Type of medium	Air		Air	Water	Silica gel
Time (days)	5	30	1	< 1	10
Mineralogy	Lead acetate	Hydrocerussite	Cerussite	Cerussite	Cerussite (hydrocerussite)
Crystal morphologies	Plate-like micro-crystals	Nano-crystals	Nano-crystals	Pseudo-hexagonal dipyramidal habit	Aggregates, skeletal crystals

drawing of orientation maps and pole figures in stereographic projection for the selected areas in a polished section of the sample. Orientation maps could be viewed along three directions in the sample: normal to the polished thin section (ND), the transverse direction (TD, corresponding to the direction along the horizontal line), and the rolling direction (RD, dip), the latter two parallel to the plane of the section. Colours in the orientation maps correspond to the diverse crystallographic directions in the orientation patterns of cerussite: [0 0 1] (red), [1 0 0] (green), [0 1 0] (blue). In the cases studied, the [0 0 1] direction was located close to one of the previous three directions of the reference system in the sample (ND, RD, or TD).

3. Computational chemistry

3.1. Theoretical background and computational details

The electronic structure of the cerussite mineral was calculated at the density functional theory (DFT) level using the ABINIT code (6.12) [25–28] and taking into account periodic boundary conditions to simulate cerussite crystals. All calculations were made with the gradient-corrected density functional of Perdew, Burke, and Ernzerhof, hereafter abbreviated PBE [29] using a norm-conserving pseudopotential generated according to the scheme of Troullier and Martins [30] for O, C, and Pb atoms. They were obtained from the Abinit GGA (PBE) repository of pseudopotential files generated with the code of the Fritz-Haber-Institute (FHI) [31]. A Monkhorst–Pack (MP) mesh was used to integrate the Brillouin zone [32]. Several convergence studies of the total energy were made in order to establish the optimised set of MP parameters and plane-wave cut-off energy that yielded an error for the total energy smaller than 0.0001 Hartree (Ha). The MP parameter varied from (4,2,4) to (8,8,8) and the plane-wave cut-off energy from 500 to 3000 eV. These studies gave an optimised set of MP and plane-wave energy cut-off of (4,2,4) and 2000 eV, respectively. The atomic coordinates of cerussite mineral were taken from Ye et al. [33]. Later, a geometric optimisation of the structure was undertaken in two steps. In the first, the atomic positions were optimised whereas the cell axes were frozen. Afterwards, the atomic positions and the cell axes were relaxed.

The electron density of the optimised structure was analysed using the quantum theory of atoms in molecules (QTAIM). This analysis was performed with the AIM tool of Abinit project [25–28].

3.2. Brief introduction to the QTAIM theory

Within the QTAIM theory, a topological analysis of the electron density is performed, which, as Bader pointed out [34,35], it is an accurate mapping of the chemical concepts of atom, bond, and structure. The principal topological properties are summarized in terms of the critical points (CPs) of $\rho(r)$, i.e. where the gradient of the electron density vanishes. Each critical point is classified in terms of the three principal curvatures of $\rho(r)$ (eigenvalues of the Hessian). At the nuclear positions, $\rho(r)$ is generally a local maximum (it is a global maximum of the electron density along the three eigenvectors of the Hessian and their corresponding eigenvalues are negative). A key CP at QTAIM analyses is the bond critical point (BCP); this is found between each pair of nuclei and has two negative curvatures and one positive, corresponding to a situation where the critical point is a maximum along two eigenvectors and a minimum along the other one. Starting from the BCP, a trajectory of $\nabla\rho(r)$ (the gradient path) is traced. The trajectory always ends in a nucleus, and then, two atoms are connected by two paths originating at the BCP and terminating at

each nuclear position. The line resulting from following these two paths is called the bond path or atomic interaction line, in which $\rho(r)$ is a maximum with respect to any neighbouring line. The presence of a bond path in an equilibrium geometry between two nuclei signifies that the atoms are bonded to one another [36]. The ellipticity of a BCP (ε) is related to the distribution of $\rho(r)$ around the BCP, indicating the anisotropy of the chemical bonding. A zero value indicates that there is no anisotropy, associated with the presence of a single bond or triple bonds. On the contrary, a non-zero value indicates an anisotropic distribution of the electron density around the BCP, associated with double bonds.

The Laplacian of the electronic density, $\nabla^2\rho(r)$, describes two extreme situations: one in which $\rho(r)$ is locally concentrated ($\nabla^2\rho(r) < 0$), and a second in which is locally depleted ($\nabla^2\rho(r) > 0$). A value of $\nabla^2\rho(r) < 0$ is associated with a covalent bonding scheme, where electronic density is shared (e.g. value for molecule C_2 is −6.55, expressed in atomic units). While in a closed-shell interaction, a value of $\nabla^2\rho(r) > 0$ is expected, where the electronic charge is separately concentrated within the atomic basins, rather than shared, as found in noble gas "repulsive" states (e.g. +1.22, in a.u., for Ar_2), ionic bonds (+7.24, in a.u., for LiF), and Van der Waals bonds between molecules (+0.65 in a.u. for $Ar-CO_2$) [36].

From the standpoint of QTAIM theory, an atom in a molecule is defined as a region delimited by a surface that is not crossed by any gradient vectors of $\rho(r)$, which is called an atomic basin. This surface is named the zero-flux surface, and mathematically is expressed in the following equation

$$\nabla^2\rho(r) \times \vec{n}(r) = 0$$

where $\vec{n}(r) = 0$ is a unit vector perpendicular to the surface at point r. A pair of atoms is bonded if their corresponding basins share zero-flux surfaces, and this condition is equivalent to the existence of a BCP and an atomic interaction line or bond path.

4. Results and discussion

4.1. Crystal-growth features

Carbonate precipitates produced by the "Dutch" method, and in particular, hydrocerussite precipitates from biomediated experiments (liquid culture medium) were poorly crystalline (Fig. 1a, Table 1). A mixture of low-crystallinity hydrocerussite and cerussite was formed when manure was used as the carbon dioxide source (Fig. 1b, Table 1); whereas cerussite occurred exclusively in
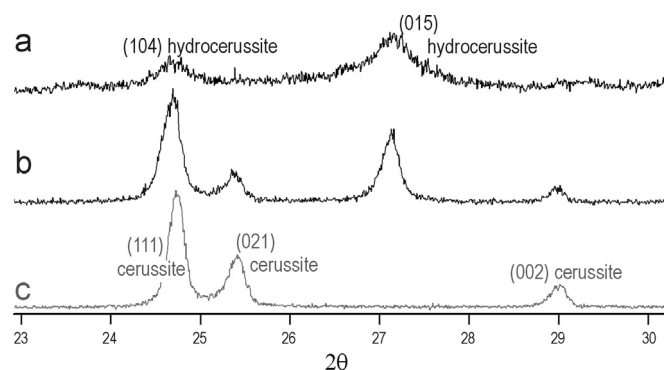

Fig. 1. X-ray diffraction (XRD) patterns of the carbonate lead formed by oxidation and carbonation processes of metallic lead with acetic acid and carbon dioxide vapours, respectively: (a) Poorly crystalline hydrocerussite formed from bacteria culture medium. (b) Mixture of hydrocerussite and cerussite obtained by using manure as the carbon dioxide source. (c) Cerussite formed from an inorganic carbon dioxide flux.

experiments with inorganic carbon dioxide flux (Fig. 1c, Table 1). Lead acetate, a sub-product of the reaction process producing the hydrocerussite through reactions 1 to 4, was determined by XRD (Table 1). It formed after the attack of acetic acid vapours onto the surface of the metallic lead and appeared as plate-like crystals with roughly micron sizes (Fig. 2a). Under SEM, vapour-growth Pb carbonates wer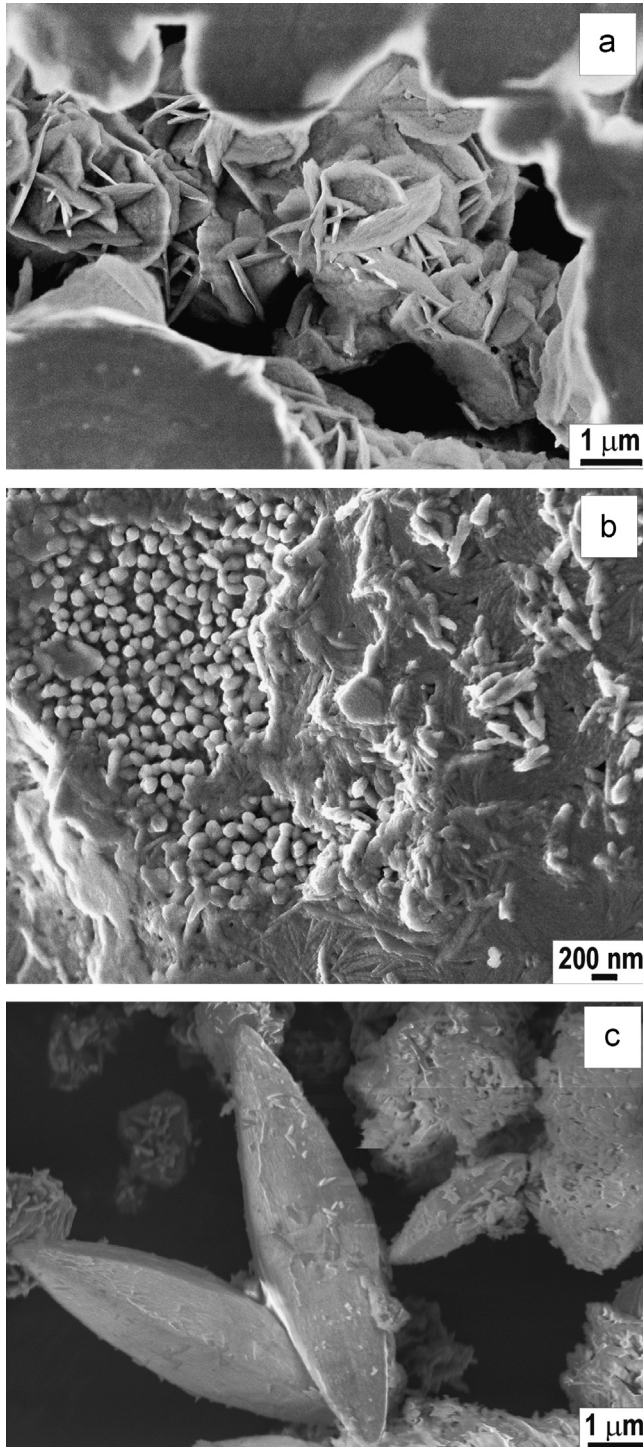e formed after the carbonation of lead acetate on the surface of the metal consisting of nanometre-sized particles with grainy surfaces (Fig. 2b).

On the other hand, lead carbonates precipitated in liquid and the gel medium consisted of idiomorphic cerussite and hydrocerussite crystals (Figs. 2c, 3, 4, Table 1). Larger cerussite crystals
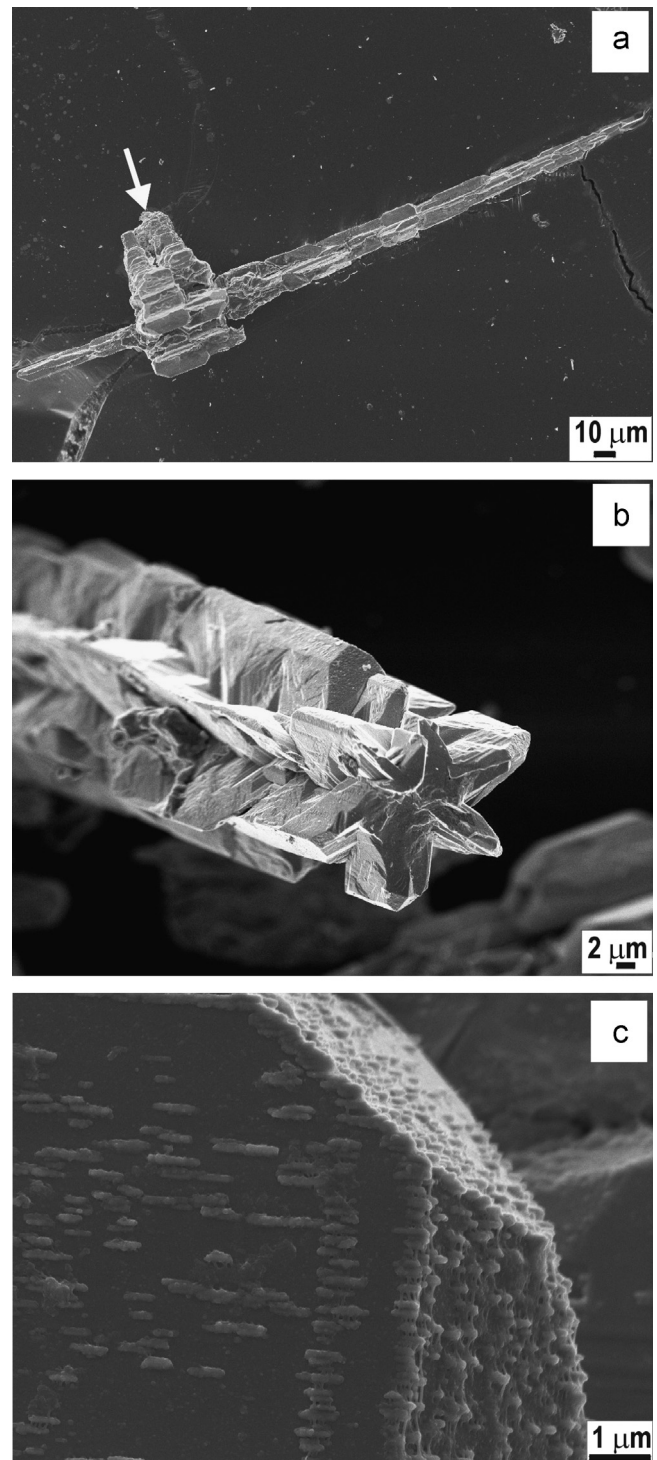
Fig. 2. (a) Secondary electron (SE) image of lead acetate crystals included in a fracture of the metallic lead and formed from acid attack of acetic vapours in the biomediated experiments. (b) SE image corresponding to the initial stages of vapour growth of lead carbonate crystals in biomediated experiments. (c) SE image of sharp pseudo-hexagonal dipyramidal cerussite crystals surrounded by a poorly crystalline precursory material precipitated from solution.

Fig. 3. SE images of gel-grown crystals of cerussite. (a) Low-magnification image showing the acicular habit and the occurrence of aggregates of cerussite crystals in the central part of the rod (arrow). (b) Truncated rod of cerussite elongated in the *c* crystallographic direction and showing a skeletal morphology composed by three cyclically twinned crystals. (c) A detail of a flat face and a rougher face with nanometre-sized rounded building blocks on their growing surface. The aggregation of the rounded particles occurs preferentially along the *c* axis of the cerussite crystal.
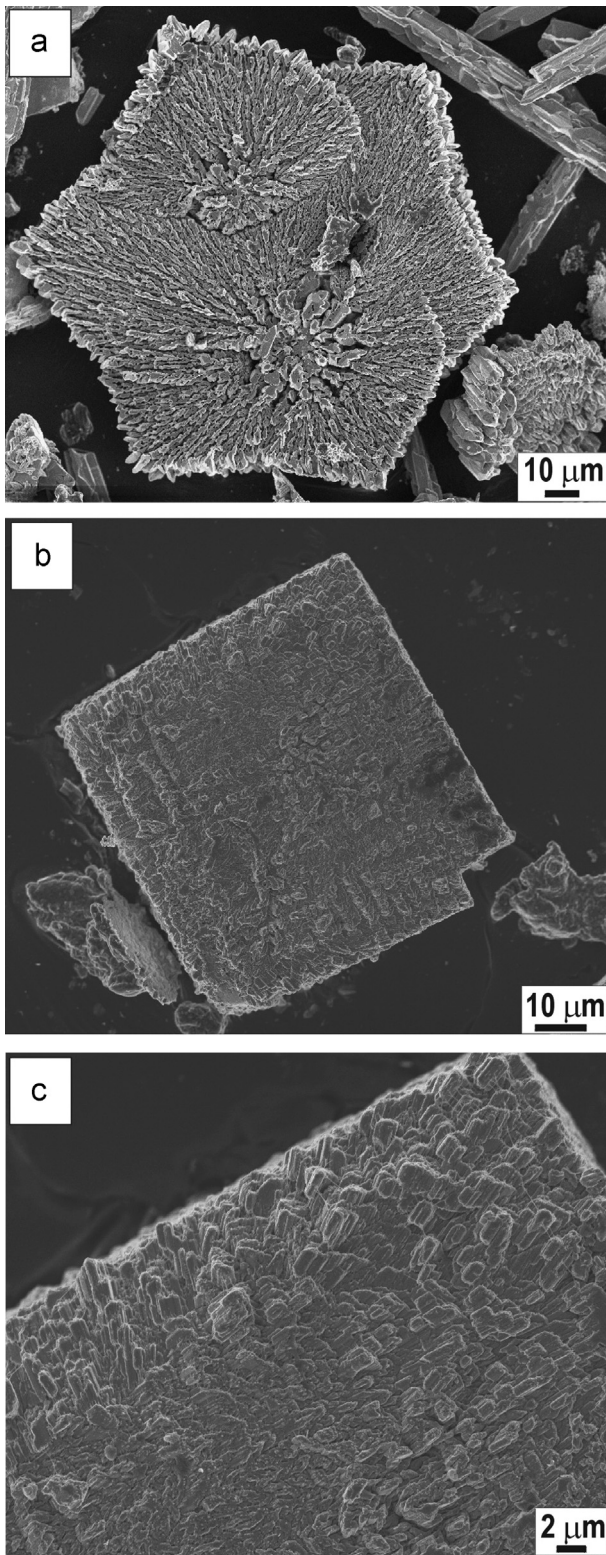
Fig. 4. SE images of gel-grown crystals. (a) Dendritic growth in a hydrocerussite crystal with ditrigonal habit. (b) Pseudo-cubic crystal shape in cerussite. (c) Detail of the surface of the crystal shown in (b), which appears to be formed by the aggregation of one-micron-sized crystallites of cerussite.

displayed sharp pseudo-hexagonal dipyramidal habits in a matrix of tiny acicular crystals on precipitating from the solution (Fig. 2c). The cerussite that formed in the silica gel usually has an acicular habit with the development of equilibrium forms {1 1 0}, {0 1 0}, and {0 2 1} (Fig. 3). Sparse hydrocerussite crystals were formed in

the region of gel column closest to the source of CO_3^{2-}. Hydrocerussite developed the following equilibrium forms: ditrigonal dipyramids {1 1 2} and {1 1 4}, in addition to the {0 0 1} basal pinacoid [37], although the examination of these crystallographical forms was usually difficult due to dendritic growth in hydrocerussite (Fig. 4a).

Crystal aggregates and twins of cerussite were also formed in the silica gel (Fig. 3a–b), in addition to pseudo-cubic morphologies, which were unexpected for cerussite crystals (Fig. 4b). These morphologies resulted from the aggregation of approximately one-micron-sized crystallites of cerussite, as confirmed by the single-point Raman spectra of Fig. 5a, which attached to the surface of the cube apparently in random orientations (Fig. 4c). However, in the pseudo-cubic crystal shape, the face of the cube was parallel to the (1 1 0) planes of the cerussite structure, as deduced from the XRD diagram of Fig. 5b corresponding to a polycrystalline sample composed by the genuine (non-milled) cubes. In the preparation of this sample the experimental design used was similar to the oriented aggregated specimen preparation used for XRD studies of clay minerals. In that case, the faces in the pseudo-cubic crystal shapes were located parallel to the surface of the zero-diffraction plate of the sample holder.

Another crystal morphology, analogous to previous pseudo-cubic crystal shape, is shown in Fig. 6. Its analysis by EBSD indicated that it consisted of a distorted single crystal with faces close to (0 1 1) and (0 −2 1) orientations. This single crystal was constituted by an assemblage of small cerussite crystallites elongated in the c direction and attached with their respective (0 1 0) pinacoidal faces approximately parallel each other (Fig. 6).
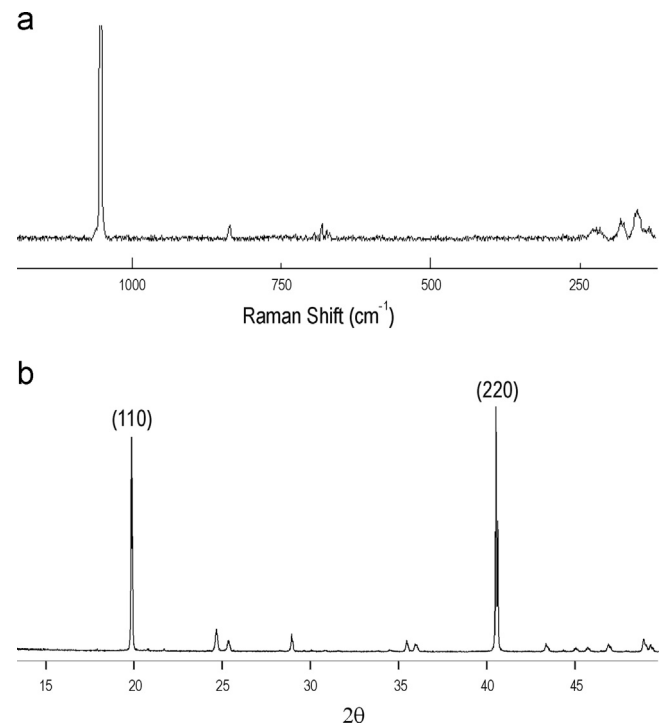

Fig. 5. (a) Raman spectrum corresponding to the cerussite crystallites that form the pseudo-cubic assembly of Fig. 4c. The assignment of the observed bands according to Martens et al. is as follows [38]: the Raman active ν1 and ν2 carbonate modes are observed at 1052 (very strong) and 837 cm^{-1} (weak). The bending modes of carbonates correspond to weak bands at 668, 674, 682, and 694 cm^{-1}. Raman active lattice vibrations appear in the low wave number region at 133, 153, 176, 181, 215, 226, and 226 cm^{-1}. (b) Preferred oriented XRD pattern from pseudo-cubic crystals such as that shown in Fig. 4b. The preferred orientation occurs because these crystals pack with the flat surfaces in a parallel orientation to the zero-diffraction plate.

Other cerussite crystal aggregates consisted of uniaxial arrays of crystals elongated in the *c* crystallographic direction (Fig. 7). Crystal coarsening gave rise to large elongated crystals along the
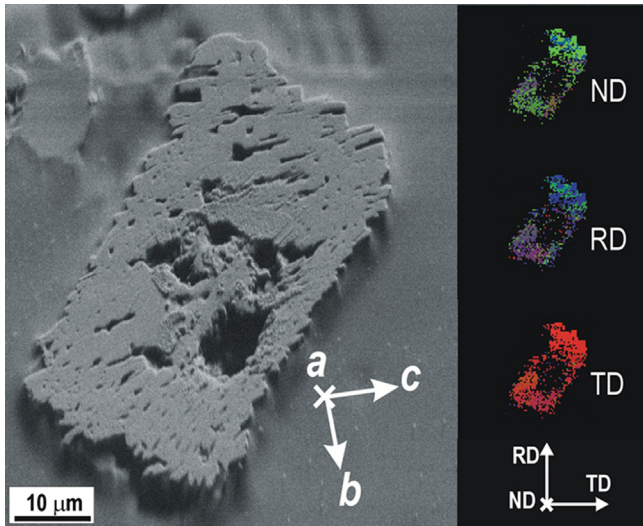

Fig. 6. EBSD study of a cerussite single crystal. Electronic image from polished section and orientation maps following sample directions of interest are shown. Colours in orientation maps indicate the crystallographic orientations for orthorhombic crystals (see Fig. 7d) of cerussite in relation to the reference system in the sample. The colour tones within crystal are not completely uniform, indicating that it is actually a distorted single crystal. Directions of the reference system in the sample (ND, RD, and TD; see section on analytical techniques) and crystallographic axis are also indicated. For this crystal the [0 0 1] direction is located close to the TD direction of the reference system in the sample.

c crystallographic direction of the aggregates (Fig. 3a). Skeletal forms with a pseudo six-fold axis were developed by these large crystals (Fig. 3b). The EBSD study showed that the skeletal forms corresponded to three cyclically twinned crystals (Fig. 8) with the dominating face {0 1 0} followed by faces {1 1 0} and {0 2 1} (compare this figure with Fig. 3b). Our observations indicate that these cerussite crystals invariably grew fastest in the *c*-direction, and to a lesser extent, in the *a*-direction.

4.2. Kinetics controls of habit in lead carbonates

Crystal growth is a complex sequential process consisting of two main stages: (1) transport of matter from medium to the surface of crystal and, (2) attachment of species on crystal surface; one of which may be the rate-limiting step [39]. In most cases, kinetic factors, such as supersaturation, determine the growth mechanism and also the crystal morphologies [40]. Sometimes precipitation takes place according to the Ostwald rule, which consists of the nucleation of unstable precursory substances that later may evolve or not towards more thermodynamically stable phases [41].

High cerussite supersaturation occurring in the solution-growth experiments resulted in the formation of cerussite crystals after the precipitation/dissolution of a poorly crystalline precursory material (Fig. 2c). The low crystallinity inferred from XRD patterns and observed in secondary electron images for Pb carbonates precipitated by the "Dutch" method (Figs. 1 and 2b) was due to the high cerussite and hydrocerussite supersaturation, resulting from: (1) the high Pb^{2+} concentration in the water vapour condensed on the surface of the metal (moisture) because of the marked solubility of precursory lead acetate in water and
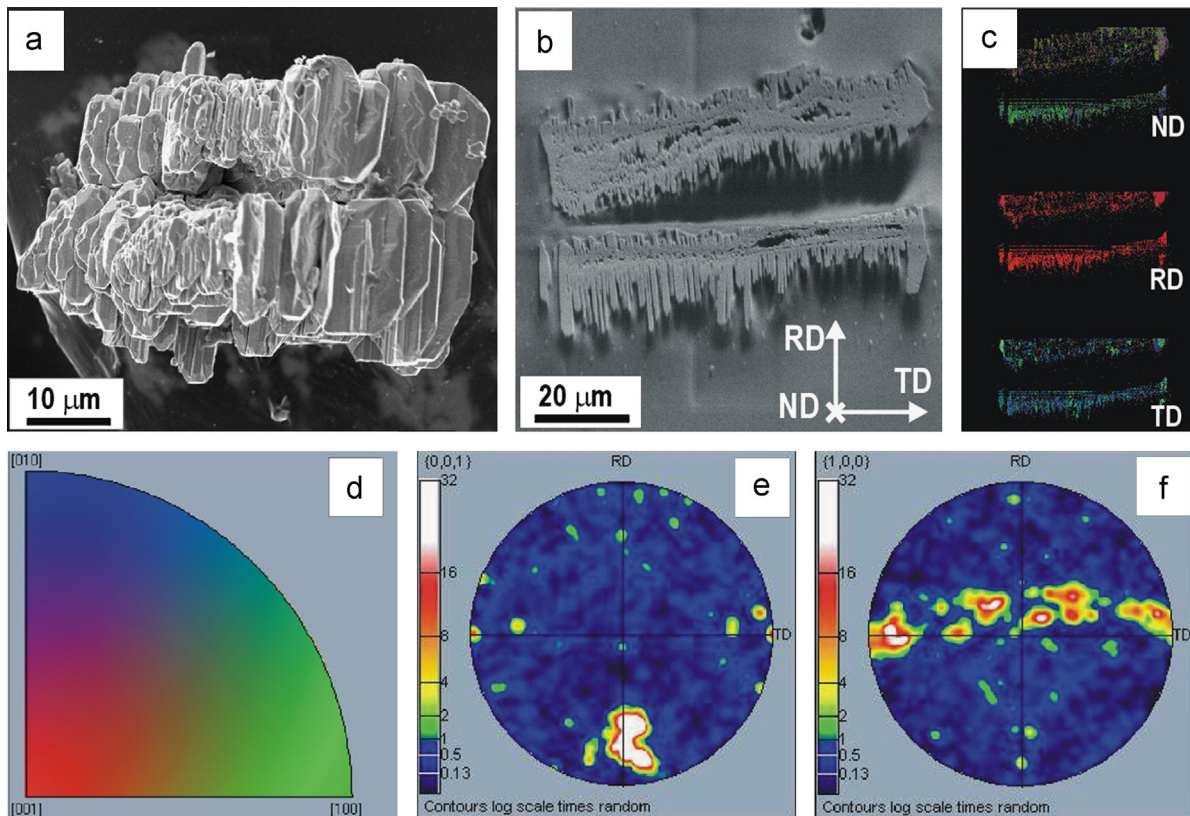

Fig. 7. (a) and (b) SE images of aggregates of cerussite crystals. The image (b) corresponds to a polished section in which the plane sample is tilted at 70° relative to normal incidence of the electron beam. Small cerussite crystallites forming the aggregates are elongated in the *c* direction and locally appear disposed with their respective (0 1 0) pinacoidal faces approximately parallel each others. (c) Orientation maps following the sample directions. In this case, the [0 0 1] direction is located close to the RD direction of the reference system in the sample, whereas [1 0 0] and [0 1 0] show random orientations. (d) Inverse pole figure for orthorhombic crystals, where the axes of the projection sphere are aligned with crystallographic directions. (e) (0 0 1) Pole figure. (f) (1 0 0) Pole figure.
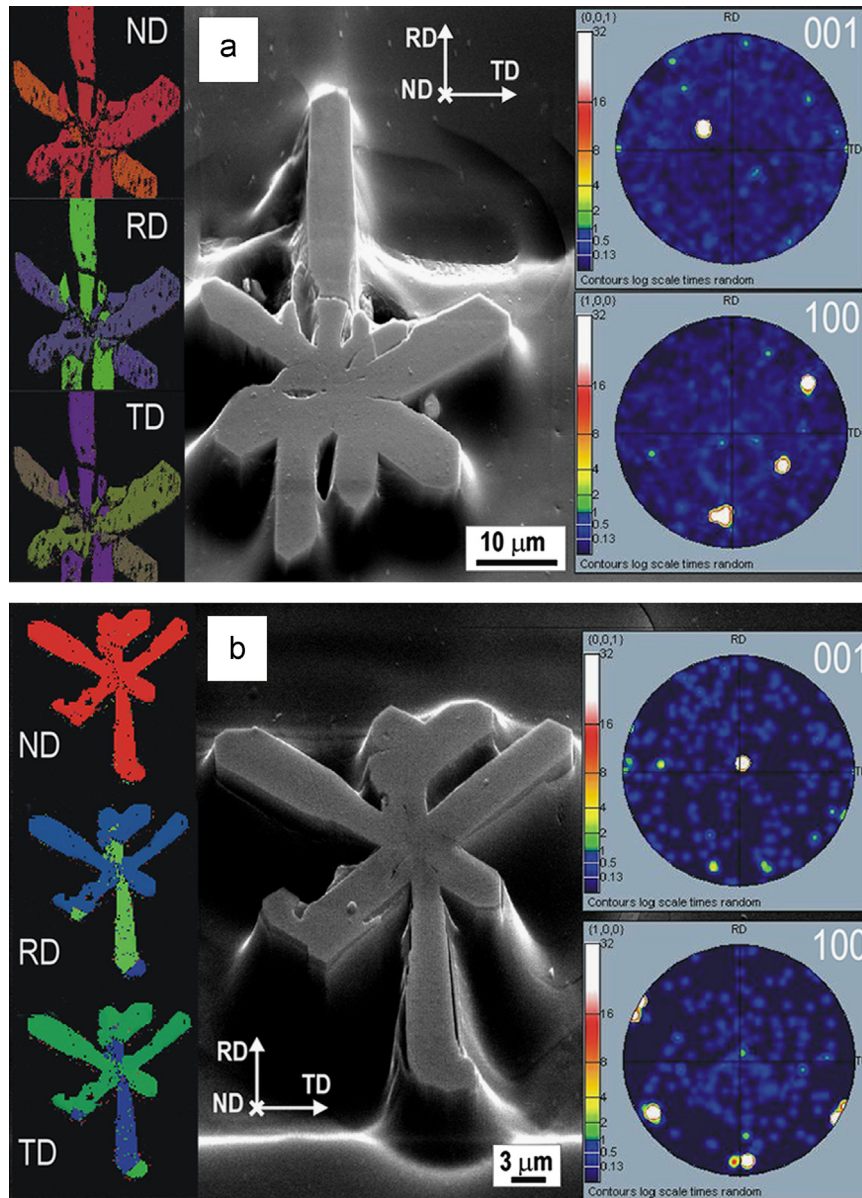
Fig. 8. (a) and (b) EBSD study of two cyclic twinning in skeletal cerussites: electronic image, orientation maps (ND, TD, and RD), and (0 0 1) and (1 0 0) pole figures are shown in both cases. In the case of (b) the [0 0 1] direction is located closer to the ND direction of the reference system in the sample than in (a). The orientation of [0 1 0] and [1 0 0] directions in the three crystals forming the cyclic twinning with respect to the reference system in the sample is also approximately the same in both cases.

moisture evaporation; and (2) the reduction of the acid character of the lead acetate–water solutions by the ambient air and the NH_3 released together with the CO_2 by the microorganisms, which increased the carbonate concentration in solution. The formation of cerussite in the inorganic vapour-assisted precipitation experiment may be related to a major CO_2 flux and to the absence of NH_3 in this case.

As opposed to vapour- and solution-growth experiments, gel-growth provided a diffusive transport, allowing the growth of larger lead carbonate crystals. Diffusion across the layer adjacent to the crystal surface produces concentration gradients due to the disappearance of the solutes at the solid/medium interface [42]. In our gel-growth experiments, the change in the local supersaturation along the solid/gel interface explains the larger skeletal crystals formed in relation to the uniaxial array of cerussite crystals (Figs. 3a and b, 7 and 8). These crystals resulted from a diffusion control of growth of cerussite crystals in the porous solid media: crystal coarsening decreased supersaturation in the areas

closest to these aggregates, and only more elongated crystals grew along the *c* crystallographic direction of the aggregates, penetrating more and more into regions of higher concentration in the gel (Fig. 3a). This process is quite similar to the well-known Berg effect and, as a result, growth of acicular morphologies with a pseudo-six-fold axis occurred within the surface-nucleation-controlled range [43].

Crystal growth in silica gels takes place under high supersaturation, also favouring the nucleation of small clusters [44,45]. Under these conditions, single-crystals may form from a meso-crystal intermediate constituted by nano-particle self-assembly [46]. In organic mesocrystals the electronic properties, such as the polarizability and the dipole moments of the molecules (inter-molecular forces) responsible for the attachment of the nano-particles, are more easily envisaged than in inorganic mesocrystals [47,48]. The pseudo-cubic morphologies of cerussite crystallites (Fig. 4b and c) and cerussite single-crystal of Fig. 6 formed from the aggregation of micro-crystals. The occurrence of weak

long-range chemical interactions between nano-crystals would explain the aggregate growth mechanism. Although the rearrangement of nano-particles in gel medium to form a regular shape seems difficult, the most defined mesocrystals are found in gels [46]. This is traditionally explained by the fact that for diffusive media, convection or turbulence throughout crystallization is suppressed, thus allowing the interaction potentials between the particles to dominate the mutual alignment of the particles. However, the arrangement process is more difficult in the case studied here because of the large size of the building blocks.

As suggested, crystals of micrometre-size form due to the high supersaturation conditions during crystal growth in gel media, decreasing the activation energy for cluster nucleation and increasing the nucleation rate in relation to the growth rate. Textural observations from secondary electron image of Fig. 4c suggests that micro-crystals became attached to the surface of the cube in random orientations. However, XRD data (Fig. 5b) indicate that the building blocks were incorporated to the crystal aggregates with their respective (1 1 0) faces approximately parallel to the cube surfaces during the self-assembly process. The pseudo-cubic morphology appears to result from a chemical recognition of (1 1 0) faces by the one-micron-sized building blocks, as indicated by our XRD experimental data (Fig. 5b). According to the Donnay–Harker and Bravais ideas [49,50], the relative importance (area) of the development of the crystal faces is on the same order as their interplanar spacing, and large and short d-spacings relate to weak and strong bonds, respectively. An equilibrium form in the case of cerussite crystals is {1 1 0} and therefore weak long-range bonds are expected perpendicular to these flat faces. The importance of weak interactions perpendicular to flat faces in aggregation-based mechanism associated with crystal coarsening has been suggested in relation to Ostwald-ripening processes for clay minerals [51,52]. All this suggests that the concept of mesocrystal needs to be revised to include new cases having more degrees of freedom in the self-assemblage process.

4.3. Long-range chemical interactions in the cerussite structure and crystal growth

In the previous section, we have dealt with the importance of weak interactions when continuous growth or two-dimensional growth mechanisms operates under high supersaturation conditions. It has led us to propose that for crystal growth relatively departed from equilibrium conditions (*i.e.* supersaturation guarantees yet the stability of planar crystal surfaces and the occurrence of crystallographically controlled interfaces) the preferred sites on the crystal surface available to atoms and molecules do not coincide with those with maximum bond strength. Therefore, weak attractive interactions should be kinetically favoured, and their prevalence under high growth-rates determined the

morphology of the cerussite crystals. As indicated above, the intermolecular forces responsible for the attachment of the nano-particles in the mesocrystals found for organic crystals are more evident than long-range chemical interactions occurring in the mesocrystals formed by inorganic compounds. In a molecular lattice a distinction between intermolecular and intramolecular bonds is easily made. In a layer lattice, such as graphite, an analogous distinction may also be made between interlayer bonds, and intralayer bonds [53]. If the homonuclear (anion–anion or cation–cation) distances within crystal lattice of inorganic ionic compounds, which are usually not considered to be chemical bonds, are treated as intermolecular bonds, the same approach as presented for a molecular lattice may be applied for inorganic ionic crystals [54].

The precipitation mechanism of lead carbonates, in solution as well as in gel-growth experiments, consists of a chemical exchange reaction among diverse soluble-salt pairs. The driving force for $PbCO_3$ crystallization is the chemical reaction between a soft acid (H_2CO_3) and an electronegative cation (Pb^{2+}) [55,56]; therefore, strong attractive forces between the CO_3^{2-} molecular group and Pb^{2+} are expected on the crystal side of the crystal-medium interface under equilibrium conditions. In this sense, preferred crystal growth along a direction observed for cyclically twinned crystals (Fig. 8) may be explained by the forces between CO_3^{2-} molecular group and Pb^{2+} (3.08 Å cation–anion distance) defining an uninterrupted chain of strong bonds along this crystallographic direction (Fig. 9a). The occurrence of a strong "crystallization pressure" derived from cation–anion interactions at the cerussite crystal–gel interface directed along the a axis agrees with the observation of etching lineations along a direction in biologically induced growth of other orthorhombic carbonates such as aragonite [57].

Aragonite-based biomaterials also constitute natural examples of the importance of weak attractions between crystal faces (in particular (0 0 1) faces of aragonite crystals) and inhibitory organic molecules in determining the morphology of crystals [58]. High growth rate along the c direction noted for the cerussite crystals that formed in our gel-growth experiments may be explained not only by the chemical interactions between carbonate and lead ions. Distances along the c direction of 3.08 Å associated with intermolecular interactions between CO_3^{2-} groups are of the same magnitude of the distances between carbonate and lead ions (3.08–3.63 Å) related to anion–cation interactions. Weak C–C atomic interactions among the CO_3^{2-} molecular groups across the shared faces of the $(CO_3)Pb_6^{+10}$ octahedra in the cerussite structure (*anti-NiAs* structure) define periodic bonding chains along the c axis (Fig. 9b).

The [0 0 1] direction in aragonite (isotypic to cerussite) was presented as an example of PBC (periodic bond chain) [59,60] resulting from a cation–anion attractive interaction described by
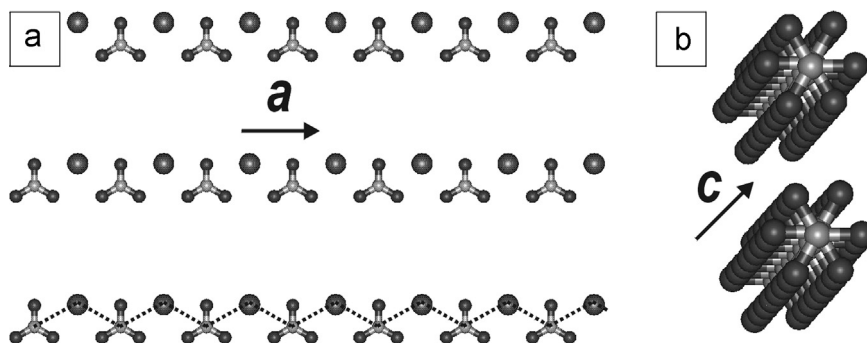

Fig. 9. Sketches of the crystal structure of cerussite showing: (a) zigzag chains –Pb–CO₃–Pb– in the [1 0 0] direction; and (b) packing of CO_3^{2-} molecular groups along the c axis defining uninterrupted chains of –C–C– bonds.

Hartman in his PhD thesis, according to the rules that he himself proposed: "For a crystal to grow in the direction of a strong bond, these bonds must form an uninterrupted chain through the structure. If a bond chain contains bonds of different types, its influence on the shape of the crystal is determined by the weakest bond present in the chain". In the zigzag arrangement defined by the alternation of carbonate and lead ions along the [0 0 1] direction in the cerussite structure, there is an alternation of short cation–anion distances (3.08–3.09 Å) and longer ones (3.44–3.63 Å). This is because the anions are not located in the centre of the $(CO_3)Pb_6^{\pm10}$ polyhedrons and they are closer to one of the layers formed by the lead ions arranged in a close hexagonal packing. Therefore, carbonate–lead ion chains are interrupted along the c axis and the preferred growth along c direction observed for the cerussite crystals must be determined by the weakest cation–anion attractive interaction corresponding to the longer anion–cation distances (3.44–3.63 Å).

For a closer look at the question related to the occurrence of stabilizing C–C interactions along c direction, we performed the topological analysis of the electron-density distributions in the cerussite-crystal structure within Bader's QTAIM theory [34,35] (Table 1). Whereas the bonding nature of the (closed-shell) carbonate–lead interactions through the O–Pb bonds is beyond any doubt, as deduced from topological properties at critical points of O–Pb bonds in Table 2, the stabilizing nature of the long C–C bonds ($ > 2.7$ Å) observed between molecules and in solids is still a subject of debate [61–63]. The existence of long-distance C–C bonds ($ > 2.9$ Å) has been explored experimentally [64] and theoretically [61–63,65,66]. Our results in Table 2 indicate that electron-density-related properties, such as those defined in the bond critical point (BCP), enabled us to find bonding interactions in the cerussite structure, and specifically, the presence of a long C–C bond connecting the CO_3^{2-} molecular groups along the c axis and defining periodic bond chains (Figs. 9b and 10).

Table 2
Electron density $\rho(r)$, its Laplacian $\nabla^2\rho(r)$, and ellipticity ε at the selected BCPs (C–C and Pb–O bonds) expressed in atomic units.

Bond	$\rho(r)$ (e/a_0^3)	$\nabla^2\rho(r)$ (e/a_0^5)	ε	Bond	$\rho(r)$ (e/a_0^3)	$\nabla^2\rho(r)$ (e/a_0^5)	ε
C5–C8	0.006	0.023	4.02	C6–C7	0.006	0.023	4.02
Pb1–O11	0.025	0.078	0.01	Pb3–O9	0.025	0.078	0.02
Pb1–O17	0.028	0.097	0.02	Pb3–O16	0.028	0.097	0.01
Pb1–O18	0.028	0.089	0.15	Pb3–O15	0.028	0.089	0.06
Pb1–O13	0.028	0.089	0.15	Pb3–O20	0.028	0.089	0.06
Pb1–O14	0.028	0.097	0.04	Pb3–O19	0.028	0.097	0.04
Pb1–O20	0.032	0.103	0.08	Pb3–O13	0.032	0.103	0.04
Pb1–O15	0.032	0.103	0.07	Pb3–O18	0.032	0.103	0.06
Pb1–O12	0.035	0.125	0.13	Pb3–O10	0.035	0.125	0.09
Pb2–O12	0.025	0.078	0.07	Pb4–O10	0.025	0.078	0.02
Pb2–O13	0.028	0.097	0.03	Pb4–O20	0.028	0.097	0.02
Pb2–O14	0.028	0.089	0.06	Pb4–O19	0.028	0.089	0.12
Pb2–O17	0.028	0.089	0.06	Pb4–O16	0.028	0.089	0.12
Pb2–O18	0.028	0.097	0.05	Pb4–O15	0.028	0.097	0.03
Pb2–O16	0.032	0.103	0.09	Pb4–O17	0.032	0.103	0.08
Pb2–O19	0.032	0.103	0.10	Pb4–O14	0.032	0.103	0.07
Pb2–O11	0.035	0.125	0.01	Pb4–O9	0.035	0.125	0.00

5. Conclusions

Crystal-growth features observed for lead carbonates depend on the kinetics of the precipitation processes and on the crystal structure. Cerussite and hydrocerussite supersaturations, controlling crystal-growth mechanisms, are achieved through diverse reactions. In biomediated and inorganic vapour-growth experiments of cerussite and hydrocerussite from metallic lead, intermediate precursory soluble salts of lead (lead acetate) must be formed. Dendritic forms, distorted single-crystals and aggregates with pseudo-cubic morphology were obtained for cerussite in silica gel using a double-diffusion arrangement.

Chemical interactions other than those occurring between nearest-neighbours may control the habit of crystals. Under high supersaturation conditions the rate of attachment of constituents along the c axis of cerussite crystals increases drastically, resulting in a fibrous habit. Fast growth along this direction of the cerussite structure is related to weak intermolecular interactions between CO_3^{2-} groups through C–C bonds in the structure of cerussite. Distances between CO_3^{2-} groups along the c direction, 3.08 Å, are of the same magnitude as the distances between carbonate and lead ions (3.08–3.63 Å). Next-nearest-neighbour distances of the same magnitude occur between the lead atoms (closely packed) along the c crystallographic in the structure of cerussite. Such structural considerations suggest that sites for surface nucleation on (0 0 1) planes under high supersaturation conditions were sites with weak bond strength.
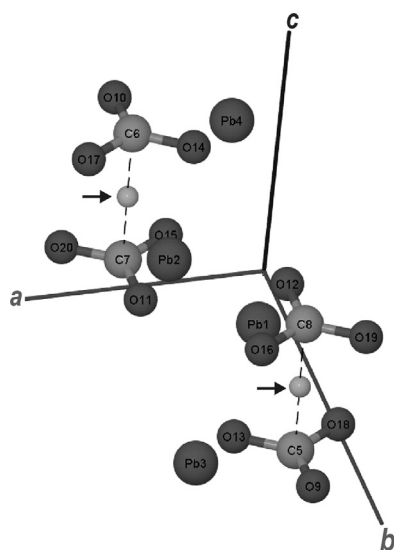
Fig. 10. Fragment torn from the extended cerussite structure with an indication of bond-critical points (arrows) between C atoms connecting CO_3^{2-} molecular groups along the c axis.

References

[1] W. Smith, A dictionary of Greek and Roman antiquities, Harper & Brothers, New York, 1843.
[2] H. Rackham, Pliny Natural History, Harvard University Press, Cambridge, 1989.
[3] M.Y. Colby, L.J.B. LaCoste, Zeitschrift für Kristallographie 84 (1933) 299–309.

[4] P. Martinetto, M. Anne, E. Dooryhe´e, P. WalterG. Tsoucaris, Acta Crystallographica Section C: Crystal Structure Communications 58 (2002) i82–i84.
[5] L.L.Y. Chang, R.A Howie, J. Zussman, Rock forming minerals, Non-Silicates; Sulphates, Carbonates, Phosphates and Halides, vol. 5B, Longman, Harlow, 1996.
[6] S.S. Jørgensen, M. Willems, AMBIO: A Journal of the Human Environment 16 (1987) 11–15.
[7] T. Nedwed, D.A. Clifford, Waste Management 17 (1997) 257–269.
[8] J.H. Colling, P.A.E. Whindcup, C.R. Hayes, Journal of the Institution of Water & Environmental Management (1987) 263–269.
[9] G.V. Korshin, J.F. Ferguson, A.N. Lancaster, Corrosion Science 42 (2000) 53–66.
[10] H. Bilinski, P. Schindler, Geochimica et Cosmochimica Acta 46 (1982) 921–928.
[11] M.A. Mercy, P.A. Rock, W.H. Casey, M.M Mokarram, American Mineralogist 83 (1998) 739–745.
[12] R.M. Garrels, American Mineralogist 42 (1957) 780–791.
[13] M. Randall, H.M. Spencer, Journal of the American Chemical Society 50 (1928) 1572–1583.
[14] J.D. Dana, A System of Mineralogy—Descriptive Mineralogy, Wiley, New York, 1868.
[15] W. Franke, M.A. Ittyachen, K.M. Pillai, Journal of Crystal Growth 51 (1981) 309–313.
[16] C.M. Pina, L. Fernández-Diaz, M. Prieto, Journal of Crystal Growth 158 (1996) 340–345.
[17] Y. Shirota, K. Niki, H. Shindo, Journal of Crystal Growth 324 (2011) 190–195.
[18] W.B. Pearson, L.D. Calvert, J. Trotter, Structure Reports, Volume 29: Metals, Inorganic and Organic Sections, International Union of Crystallography, Utrecht, 1964.
[19] J. Trotter, L.D. Calvert, Structure Reports, Volume 40 A: Metals and Inorganic Section, International Union of Crystallography, Utrecht, 1968.
[20] G.V. Korshin, J.F. Ferguson, A.N. Lancaster, Water Research 39 (2005) 811–818.
[21] M. Bucca, M. Dietzel, J. Tang, A. Leis, S.J. Köhler, Chemical Geology 266 (2009) 143–156.
[22] A.K. De, Inorganic Chemistry, New Age International Publications, New Delhi, 2003.
[23] L. Fernández-Díaz, A. Putnis, M. Prieto, C.V. Putnis, Journal of Sedimentary Research 66 (1996) 482–491.
[24] J.D. Martín, Using XPowder a Software Package for Powder X-ray Diffraction Analysis (⟨http://www.xpowder.com⟩), 2004.
[25] X. Gonze, B. Amadon, P.M. Anglade, J.M. Beuken, F. Bottin, P. Boulanger, F. Bruneval, D. Caliste, R. Caracas, M. Cote, T. Deutsch, L. Genovese, P. Ghosez, M. Giantomassi, S. Goedecker, D.R. Hamann, P. Hermet, F. Jollet, G. Jomard, S. Leroux, M. Mancini, S. Mazevet, M.J.T. Oliveira, G. Onida, Y. Pouillon, T. Rangel, G.M. Rignanese, D. Sangalli, R. Shaltaf, M. Torrent, M.J. Verstraete, G. Zerah, J.W. Zwanziger, Computer Physics Communications 180 (2009) 2582–2615.
[26] X. Gonze, G.M. Rignanese, M. Verstraete, J.M Beuken, Y. Pouillon, R. Caracas, F. Jollet, M. Torrent, G. Zerah, M. Mikami, P. Ghosez, M. Veithen, J.Y. Raty, V. Olevano, F. Bruneval, L. Reining, R. Godby, G. Onida, D.R. Hamann, D.C. Allan, Zeitschrift für Kristallographie 220 (2005) 558–562.
[27] The ABINIT Code is a Common Project of the Université Catholique de Louvain, Corning Incorporated, and Other Contributors (URL ⟨http://www.abinit.org⟩).
[28] P.M. Anglade, X. Gonze, Physical Review B: Condensed Matter 78 (2008) 45126–45136.
[29] J.P. Perdew, K. Burke, M. Ernzerhof, Physical Review Letters 77 (1996) 3865–3868.
[30] N. Troullier, J.L. Martins, Physical Review B: Condensed Matter 43 (1991) 1993–2006.
[31] M. Fuchs, M. Scheffler, Computer Physics Communications 119 (1999) 67–98.
[32] H.J. Monkhorst, J.D. Pack, Physical Review B: Condensed Matter 13 (1976) 5188–5192.
[33] Y. Ye, J.R. Smyth, P. Boni, American Mineralogist 97 (2012) 707–712.
[34] R.F.W. Bader, Atoms in Molecules: A Quantum Theory, Clarendon Press, Oxford, 1990.
[35] R.F.W. Bader, Chemical Reviews 91 (1991) 893–928.
[36] R.F.W. Bader, Journal of Physical Chemistry A 102 (1998) 7314–7323.
[37] S Weber, Journal of Applied Crystallography 32 (1999) 375, JCrystal Crystal Shape Editor/Viewer 1.0.5 © JCrystalSoft, 2005–2011.
[38] W.N. Martens, L. Rintoul, J.T. Kloprogge, R.L. Frost, American Mineralogist 89 (2004) 352–358.
[39] A.E. Nielsen, J. Christoffersen, The mechanism of crystal growth and dissolution, in: G.H. Nancollas (Ed.), Biological Mineralization and Demineralization, Springer-Verlag, New York, 1982, pp. 37–77.
[40] I. Sunagawa, Morphology of Crystals, Terra Scientific Publishing Company, Tokyo, 1987.
[41] T. Ogino, M.T. Suzuki, K. Sawada, Geochimica et Cosmochimica Acta 51 (1987) 2757–2767.
[42] J.M. García-Ruiz, Methods in Enzymology 368 (2003) 130–154.
[43] R.J. Kirkpatrick, Kinetics and crystallization of igneous rocks, in: A.C. Lasaga, R.J. Kirkpatrick (Eds.), Reviews in Mineralogy and Geochemistry, 8, MSA, Washington, 1984.
[44] A. Putnis, M. Prieto, L. Fernandez-Diaz, Geological Magazine 132 (1995) 1–13.
[45] O. Grassmann, R.B. Neder, A. Putnis, P. Löbmann, American Mineralogist 88 (2003) 647–652.
[46] H. Cölfen, M. Antonietti, Angewandte Chemie International Edition 44 (2005) 5576–5591.
[47] S. Wohlrab, N. Pinna, M. Antonietti, H. Cölfen, Chemistry—A European Journal 11 (2005) 2903–2913.
[48] A. Taden, K. Landfester, M. Antonietti, Langmuir 20 (2004) 957–961.
[49] J.D.H. Donnay, D. Harker, American Mineralogist 22 (1937) 446–447.
[50] J.M. Buerger, American Mineralogist 32 (1947) 593–609.
[51] P.H. Nadeau, Clay Minerals 20 (1985) 499–514.
[52] D.D. Eberl, J. Srodon, M. Kralik, B.E. Taylor, Z.E. Peterman, Science 248 (1990) 474–477.
[53] V. Gutmann, H. Mayer, Structure and Bonding 31 (1976) 49–66.
[54] V. Gutmann, The Donor–Acceptor Approach to Molecular Interactions, Plenum Press, New York, 1978.
[55] R.G. Pearson, Science 151 (1966) 172–177.
[56] J.K. Burdett, T.J. MacLarnan, American Mineralogist 69 (1984) 601–621.
[57] H. Mutvei, Zoologica Scripta 7 (1978) 287–296.
[58] A.G. Checa, A. Sánchez-Navas, A. Rodríguez-Navarro, Crystal Growth & Design 9 (2009) 4574–4580.
[59] P. Hartman, W.G. Perdok, Acta Crystallographica 8 (1955) 49–52.
[60] P. Hartman, P. Bennema, Journal of Crystal Growth 49 (1980) 145–156.
[61] I. Vidal, S. Melchor, J.A. Dobado, Journal of Physical Chemistry A 112 (2008) 3414–3423.
[62] I. Alkorta, F. Blanco, J. Elguero, J.A. Dobado, S.M. Ferrer, I. Vidal, Journal of Physical Chemistry A 113 (2009) 8387–8393.
[63] Y.V. Nelyubina, K.A. Lyssenko, Chemistry—A European Journal 18 (2012) 12633–12636.
[64] J.J. Novoa, P. Lafuente, R.E.D. Sesto, J.S. Miller, Angewandte Chemie International Edition 40 (2001) 2540–2545.
[65] R.E.D. Sesto, J.S Miller, P. Lafuente, J.J. Novoa, Chemistry—A European Journal 8 (2002) 4894–4908.
[66] I. García-Yoldi, F. Mota, J.J. Novoa, Journal of Computational Chemistry 28 (2007) 326–334.